Graphene Nanoribbon Quantum-Well Interband and Intersubband Photodetector

Atanu K. Saha, *Member, IEEE*, Gobinda Saha, *Student Member, IEEE*, and ABM Harun-ur Rashid, *Senior Member, IEEE*

Abstract— 1-D quantum-well (QW) formation and energy state confinement in armchair graphene nanoribbon (A-GNR) heterostructures have been studied. A photodetector device structure based on A-GNR-QWs has been proposed to incorporate both interband and intersubband optical transition using a back-gate potential. Photocurrent, dark current, and quantum efficiency of different A-GNR-QW photodetector structures are studied using self-consistent simulation between nonequilibrium Green's function formalism including electron–photon interaction and Poisson's equation. Optical detection from short-wavelength infrared to ultraviolet range has been observed having a tunable feature, which makes our device a promising candidate for future optoelectronics.

Index Terms— Graphene nanoribbon (GNR), interband, intersubband, photodetector, quantum well (QW).

I. INTRODUCTION

GRAPHENE nanoribbon (GNR), nanopatterned 2-D hexagonal lattice of carbon, is recently going through extensive research due to its remarkable electronic [1], [2] and optical properties [3]–[5]. Graphene's suitability as a photodetector was first demonstrated in [6]. Photocurrents for single/bilayer graphene interfaces [7], graphene p-n junctions [8], and hybrid graphene–quantum dot phototransistors [9] have also been reported. Unlike graphene, which is a zero bandgap material, depending on the edge geometry, armchair GNRs (A-GNRs) can have finite bandgap, thus exhibiting semiconducting behavior [10], [11].

Modern high-speed optoelectronic devices require different semiconductor heterostructures, which are usually grown as stacking crystalline materials of different electronic bandgaps. However, such structures require complex fabrication techniques (e.g., molecular beam epitaxy and chemical vapor deposition) to ensure sharp lattice-matched 2-D interfaces. In this context, intra-GNR heterostructures might open up a new dimension as structural variations of A-GNRs allow molecular-scale bandgap tuning through 1-D quantum confinement [12], [13]. The formation of 1-D quantum-well (QW)

and resonant tunneling phenomena, involving edge modulation and composition modulation of A-GNR-based heterostructures, has been investigated through the first-principle calculations [14]. Recent advances in material growth and fabrication techniques have made it possible to realize GNR heterojunctions with lateral dimensions below 2 nm [15]. More recently, edge-modulated A-GNRs at subnanometer length scale have been fabricated using bottom-up synthesis technique [16], which demonstrated molecular bandgap engineering, including type-I heterojunction behavior. Graphene photodetectors [17] and A-GNR superlattice-based photodetectors [18] have been studied numerically. However, simulation-based study on A-GNR QW structures as interband and intersubband photodetectors is yet to be done. Therefore, the investigation of the quantum confinement and optical properties of such structures along with their performance as photodetection devices is a highly appealing prospect for future optoelectronics.

Here, in this paper, we have investigated energy state confinement in intrinsic A-GNR-QW through numerical simulation using a suitable device structure to assess its performance as a photodetector. The effects of different structural parameters on such confinement have also been studied. Optical ranges, photocurrent, quantum efficiency (Q.E.), and dark current are also studied through quantum transport formalism coupled with electron–photon interaction.

The A-GNR-QW photodetector device structure is shown in Section II. The simulation procedure is described in Section III. The simulation results are presented and discussed in Section IV, and the conclusion is presented in Section V.

II. DEVICE STRUCTURE

Device structure along with the photosensitive A-GNR channel is shown in Fig. 1(a). A back gate is used to control the interband-to-intersubband transitions. Silicon dioxide is used as gate oxide with the oxide thickness of 15 nm. The incident light is assumed to be monochromatic with the electric field associated with the light is polarized along the channel direction. Photodetection layer, in Fig. 1(a), is designed utilizing peculiar electronic properties of A-GNRs. Depending on the number of carbon atoms, N, along the ribbon width, three distinct groups: 1) $N = 3p$; 2) $N = 3p + 1$; and 3) $N = 3p + 2$ (where p is a positive integer) of A-GNRs are defined. Within each group bandgap, E_g decreases with the increasing ribbon width with the superimposed oscillating behavior [19].
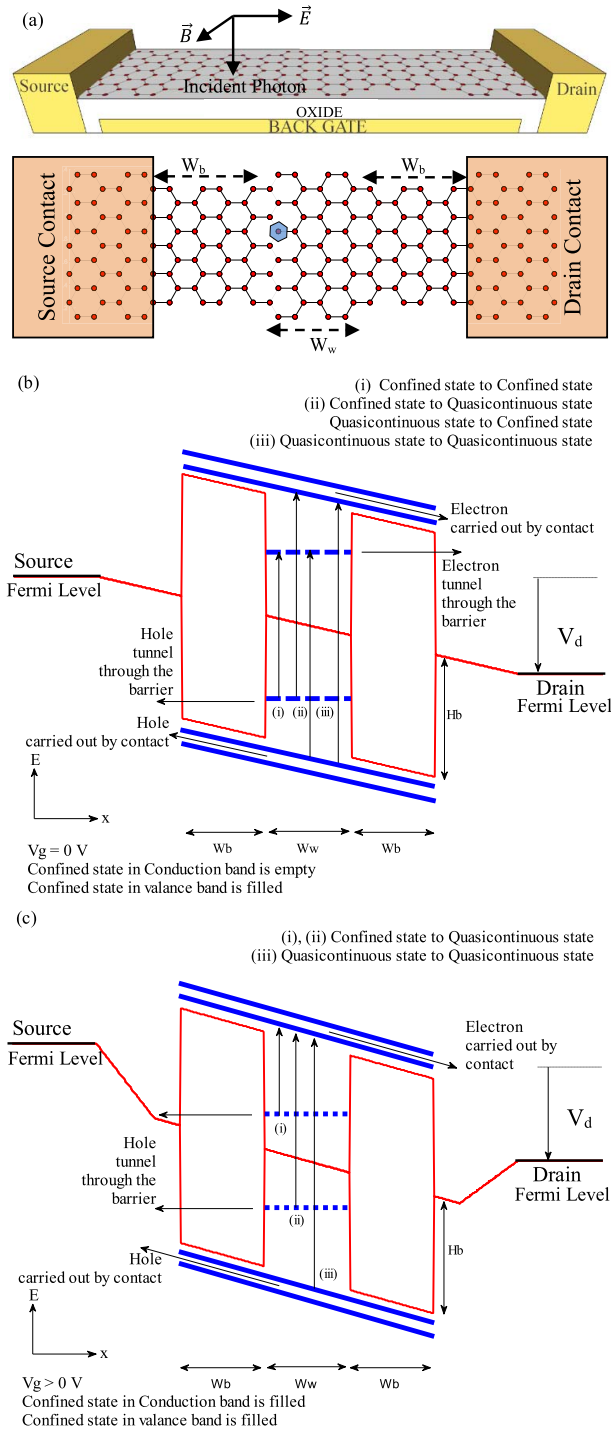
Fig. 1. (a) Device structure of A-GNR-QW photodetector with a back gate. Different regions of A-GNR-QW structure-1 have been shown. Effective area per atomic site is shown by a blue transparent hexagon, which is $a = (\sqrt{3}/2)a_{c-c}^2$ and $a_{c-c} = 0.142$ nm. (b) Energy band diagram (arbitrary) of an interband A-GNR-QW photodetector. Different types of transitions are shown when the device is under positive bias at drain contact with a back-gate voltage, $V_g = 0$ V. (c) Energy band diagram (arbitrary) of an intersubband A-GNR-QW photodetector. Different types of transitions are shown when the device is under positive bias voltage at drain contact along with the positive back-gate voltage.

When ideal A-GNR heterojunctions are formed by a sequence of ribbons belonging to different groups, for Fig. 1(a), $N_b = 9$ (barrier)/$N_w = 11$ (well)/$N_b = 9$ (barrier),

the bandgap difference between $N_b = 9$ ($E_g = \sim 0.95$ eV) and $N_w = 11$ ($E_g = \sim 0$ eV) acts as a confining potential for the $N_w = 11$ region, giving rise to an effective 1-D potential well. Due to this confining potential, energy states of different nature [e.g., confined states (inside well region) and quasi-continuous states (near continuum level)] are created in the well region. Once the constituents of the heterostructure are defined, the number and nature of states created in the well region will depend on both the barrier width W_b and the well width W_w. The source and drain contacts are also made of A-GNR of $N = 11$, ensuring smooth interface to enable negligible contact resistance.

Energy band diagrams in Fig. 1(b) and (c) explain the operation principle of the designed photodetector under specific bias conditions. For zero back-gate voltage and small positive drain bias voltage [Fig. 1(b)], energy states in the valence band (VB) will be completely occupied, and energy states in the conduction band (CB) will be completely empty. Hence, for the incident photons with particular energies, we will observe electron transitions from: (i) confined state to confined state; (ii) confined state to quasi-continuous state or vice versa; and (iii) quasi-continuous state to quasi-continuous state. As for all of these cases electron would go from the VB to the CB, under a specified bias condition, the device will act as an interband photodetector. When a positive back-gate voltage is applied so that the first confined state in the CB becomes populated [Fig. 1(c)], instead of confined state-to-confined state transition, we would observe electron transitions from the confined state of CB to the quasi-continuous state of CB for relatively lower energy photons. At higher photon energies, transitions are still of interband nature. Hence, at a certain back-gate voltage, the device can also act as an intersubband photodetector for lower energy photons.

III. SIMULATION PROCEDURE

A. Quantum Transport (NEGF Formalism)

To obtain photocurrent, quantum transport equation with electron–photon interaction is solved using non-equilibrium green's function (NEGF) formalism [20]. In order to incorporate the charging effects and to obtain built-in electric field, Poisson's equation and the transport equation are self-consistently solved. Under NEGF formalism, the carrier dynamics is described as retarded Green's function, G^R. At steady-state condition, the function can be written as

$$G^R(E) = \left[(E + i\eta)I - H_0 - \Sigma_S^R - \Sigma_D^R - \Sigma_{\text{ph}}^R\right]^{-1} \quad (1)$$

where H_0 is the device Hamiltonian, and $\Sigma_{S(D)}^R$ is retarded self-energy term due to the source (drain) contact. The effects of electron–photon interaction on carrier dynamics are incorporated as an interaction self-energy term Σ_{ph}^R. The effect of electron–phonon and electron–electron interactions can be included by adding additional self-energy terms [21] in (1), which are omitted for simplicity. I is the identity matrix, and η is a small number to enable the energy-level broadening effect. Real part of Σ_{ph}^R can be neglected as it does not change

the photon absorption and emission rate [22]. Therefore, taking only the imaginary part

$$\Sigma_{ph}^R \approx -\frac{i}{2}\Gamma_{ph} \quad (2)$$

where Γ_{ph} is the energy-level broadening function due to electron–photon interaction and can be calculated as

$$\Gamma_{ph} = \Sigma_{ph}^{in} + \Sigma_{ph}^{out} \quad (3)$$

where Σ_{ph}^{in} and Σ_{ph}^{out} are the electron in-scattering and out-scattering functions due to photon interaction, respectively, and are defined as

$$\Sigma_{ph}^{in}(E) = (N_{ph} + 1)MG^n(E + E_{ph})M^\dagger$$
$$+ N_{ph}MG^n(E - E_{ph})M^\dagger \quad (4)$$
$$\Sigma_{ph}^{out}(E) = (N_{ph} + 1)MG^p(E - E_{ph})M^\dagger$$
$$+ N_{ph}MG^p(E + E_{ph})M^\dagger \quad (5)$$

where N_{ph} is the number of incident photons, and $E_{ph}(= \hbar\omega)$ is the photon energy. The first term in (4) and (5) denotes stimulated and spontaneous photon emission, and the second term denotes photon absorption. The term M incorporates electron–photon interaction, which will be elaborated in Section III-B. The electron and hole statistics are described by correlation functions as

$$G^n(E) = G^R(E)\left[\Sigma_S^{in} + \Sigma_D^{in} + \Sigma_{ph}^{in}\right]G^{R^\dagger}(E) \quad (6)$$

$$G^p(E) = G^R(E)\left[\Sigma_S^{out} + \Sigma_D^{out} + \Sigma_{ph}^{out}\right]G^{R^\dagger}(E). \quad (7)$$

The contact in/out-scattering terms are calculated from the energy-level broadening function, $\Gamma_{S(D)} = i[\Sigma_{S(D)}^R - \Sigma_{S(D)}^{R^\dagger}]$, due to the source (drain) contact using the following set of equations:

$$\Sigma_S^{in} = f_S\Gamma_S, \quad \Sigma_D^{in} = f_D\Gamma_D, \quad \Sigma_S^{out} = (1 - f_S)\Gamma_S$$
$$\Sigma_D^{out} = (1 - f_D)\Gamma_D$$

where f_S and f_D are the source and drain Fermi functions, respectively. Density of states (DOS) at the jth atomic site can be defined as

$$\rho_j(E) = \frac{1}{2\pi}A_{j,j}(E) \quad (8)$$

where $A = i(G^R - G^{R^\dagger})$ is called spectral function. Then, electron (hole) density at the jth atomic site can be calculated as follows:

$$n_j^{e(p)} = \frac{1}{\pi}\int_{E_{nj}(\infty)}^{\infty(E_{nj})} G_{j,j}^{n(p)}(E)dE \quad (9)$$

where E_{nj} is the charge neutrality point [23] at the jth atomic site and calculated by evaluating two integrals over DOS at each atomic site using a trial energy value, E_{nj} as upper bound for valence states and lower bound for conduction states in search of equal distribution. The electrostatic potential distribution is determined using Poisson's equation as

$$\nabla^2 U_j = \frac{q(n_j^e - n_j^h)}{\varepsilon a\Delta z} \quad (10)$$

where U_j is the Hartree potential at the jth atomic site, ε is the permittivity of channel material, a is the effective

TABLE I
THIRD NEAREST TIGHT-BINDING PARAMETERS

Position	ϵ_c(eV)	t_1(eV)	t_2(eV)	t_3(eV)
Inside	0	-2.78	-0.15	-0.095
Edge	0	-2.97	-0.2	-0.080

area per atomic site and z-axis grid spacing $\Delta z = 0.5a_{c-c}$. The equation is solved under 3-D discretization using the finite-difference method. For source, drain, and gate contacts, boundary condition is Dirichlet (as the potential is fixed in contacts). In addition, in open faces of GNR sheet and oxide, the boundary condition is Neumann (open boundary).

B. Tight-Binding Description

The atomistic real-space description of GNR is depicted by the third nearest tight-binding parameters; therefore, the device Hamiltonian can represent the $\pi^* - \pi$ electrons effectively. To incorporate the effects of bond relaxation in edge carbon atoms [10], different sets of tight-binding parameters are used for them, assuming the atoms are hydrogen passivated. The parameters are extracted from comparing DFT-based band-structure calculation [10], and are given in Table I. Here, ϵ_c is on-site potential, and t_j are the tight-binding hopping parameters for the jth nearest neighbor in C–C bond.

The tight-binding description turns the device Hamiltonian H_0 [24] into an $n \times n$ matrix, where n is the total number of carbon atoms within the corresponding GNR structure. Each element of this matrix is represented by $\langle l|\hat{H}_0|m\rangle$ which is tight-binding energy between the lth and the mth atomic sites.

The above-mentioned term M also becomes an $n \times n$ matrix, where each element of the matrix is represented by [25], [26]

$$M_{l,m} = (x_m - x_l)\frac{iq}{\hbar}\left(\frac{\sqrt{\varepsilon_r\mu_r}}{2N_{ph}\omega^2\varepsilon c}p_{op}\right)^{1/2}\langle l|\hat{H}_0|m\rangle \quad (11)$$

where x_m denotes the position in the x-direction for the carbon atom at the mth site, ε_r and μ_r are relative permittivity and permeability of GNR, respectively. P_{op} is the incident optical power density, and c is the speed of light.

C. Self-Consistent Simulation

Contacts are assumed to be semi-infinite, and the contact self-energy terms are calculated using the standard iterative approach [27]. At the starting of self-consistent iteration, Σ_{ph}^R and $\Sigma_{ph}^{in(out)}$ are assumed to be empty matrices. Then, using (1), (6), (7), and (9), G^R, G^n, G^p, and $n_j^{e(p)}$ are calculated which provide update on Σ_{ph}^R and $\Sigma_{ph}^{in(out)}$ through (4) and (5). These new self-energies are again used to find new values of carrier density, $n_j^{e(p)}$, and the iteration is continued until the difference in carrier density evaluated in two successive iteration steps is less than a given tolerance value (10^{-4}).

To update the initial Hartree potential, U_j at the jth atomic site in the device Hamiltonian Poisson's equation is solved in
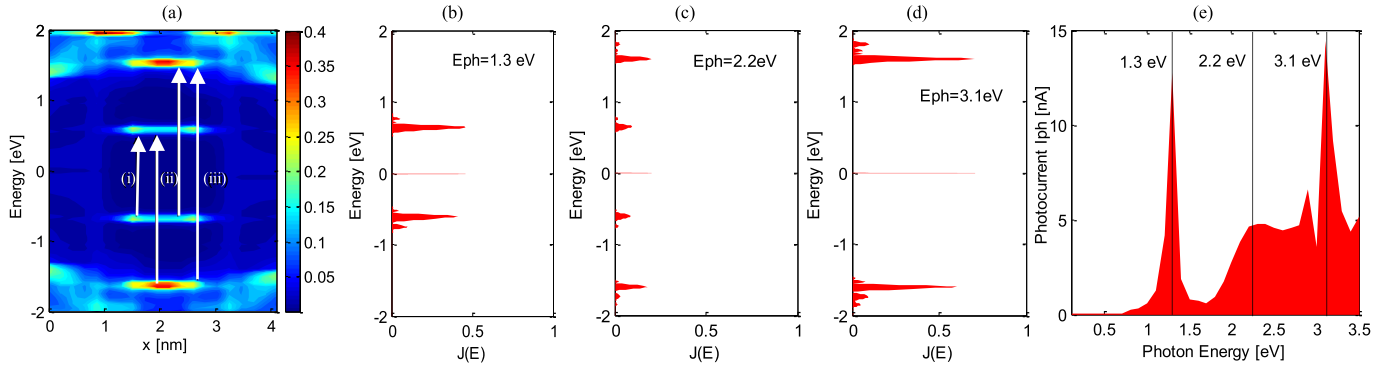
Fig. 2. (a) DOS (states per atomic site) of A-GNR-QW structure-1 along the device length. DOS is represented by averaging over site contributions at atomic sites with the same x-coordinate. Different optical transitions are shown as (i)–(iii). (b)–(d) Normalized photocurrent spectrum due to photon energy of 1.3, 2.2, and 3.1 eV, respectively. (e) Photocurrent response of the structure (at $V_g = 0$ V, $V_d = 0.1$ V, and $P_{op} = 1000$ W/m^2).

an additional self-consistent loop using the carrier densities from NEGF transport equations.

Once convergence is achieved, photocurrent and dark current spectra are computed as

$$I_{ph}(E) = \frac{2q^2}{h}\text{Trace}\left[\Gamma_D G^R \Sigma_{ph}^{in} G^{R\dagger}\right] \qquad (12)$$

$$I_{dark}(E) = \frac{2q^2}{h}\text{Trace}\left[\Gamma_D G^R \Gamma_S G^{R\dagger}\right] \qquad (13)$$

where h is Planck's constant. The current is obtained by integrating current spectrum in (12) and (13) over the energy range.

IV. RESULTS AND DISCUSSION

Photodetector for the specified geometry in Fig. 1(a) is simulated under the formalism to calculate the DOS, photocurrent, and dark current. The calculations are performed at 300 K for the optical power density of 1000 W/m^2. Fig. 2(a) shows the DOS of the device for zero back-gate voltage (for interband transitions) and 0.1 V bias voltage at the drain contact. Since the system is open, there is no true bound state in the well region. The formalism only considers states (e.g., confined states and quasi-continuous states) which contribute to the current through coupling themselves with the extended states of finite amplitude in the contacts. Different optical transitions [as shown in Fig. 1(b)] are represented as (i), (ii), and (iii) in Fig. 2(a). Normalized photocurrent density, J, as a function of energy at the middle of the well (at $x = \sim 2$ nm) corresponding to those optical transitions (at particular photon energies) is also shown in Fig. 2(b)–(d). From these results, it is apparent that the CB electrons and VB holes contribute in the photocurrent. This is due to the fact that when a photon with particular energy incidents on the device, an electron is photoexited from the filled VB state, leaving a hole behind. This electron then tunnels out of the well from the CB state to the drain contact, producing electron conduction current. While another electron from the source contact fills the vacant state in the VB, producing hole conduction current. The summation of electron and hole current contributions, i.e., total photocurrent, is constant over the length of the device, obeying current conservation [28],
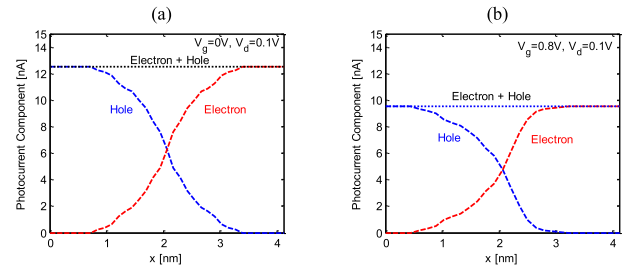

Fig. 3. Electron and hole component of photocurrent along x-direction for (a) interband transition at $E_{ph} = 1.3$ eV and (b) intersubband transition at $E_{ph} = 1$ eV for A-GNR-QW structure-1.
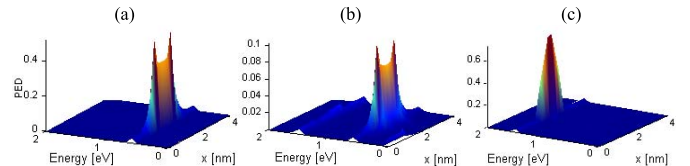

Fig. 4. PED (per atomic site) at incident photon energy of (a) 1.3, (b) 2.2, and (c) 3.1 eV.

but individually they increase toward the respective contacts. This characteristic is shown in Fig. 3(a), where photocurrent due to electron and hole components is shown separately for A-GNR-QW structure-1 at $E_{ph} = 1.3$ eV, and total photocurrent is found constant along the x-direction. Photocurrent response of the device for different photon energies is shown in Fig. 2(e). The first peak in this spectrum occurs at a photon energy of 1.3 eV corresponding to the transition marked is (i) in Fig. 2(a), which is expected as the separation between the confined states in the VB and CB as ~ 1.3 eV. From the spectrum, two additional peaks are observed at photon energies of 2.2 and 3.1 eV corresponding to the optical transitions (ii) and (iii), respectively. Photoresponse for transition (i) is sharper than for transition (iii), and the magnitude of the photocurrent is slightly larger in (iii) than in (i). This can be explained from photogenerated electron density (PED) in the CB for different incident photon energies, as shown in Fig. 4. PED for incident photon energy $E_{ph} = 3.1$ eV [in Fig. 4(c)] is larger than PED for $E_{ph} = 1.3$ eV [in Fig. 4(a)], which results in larger
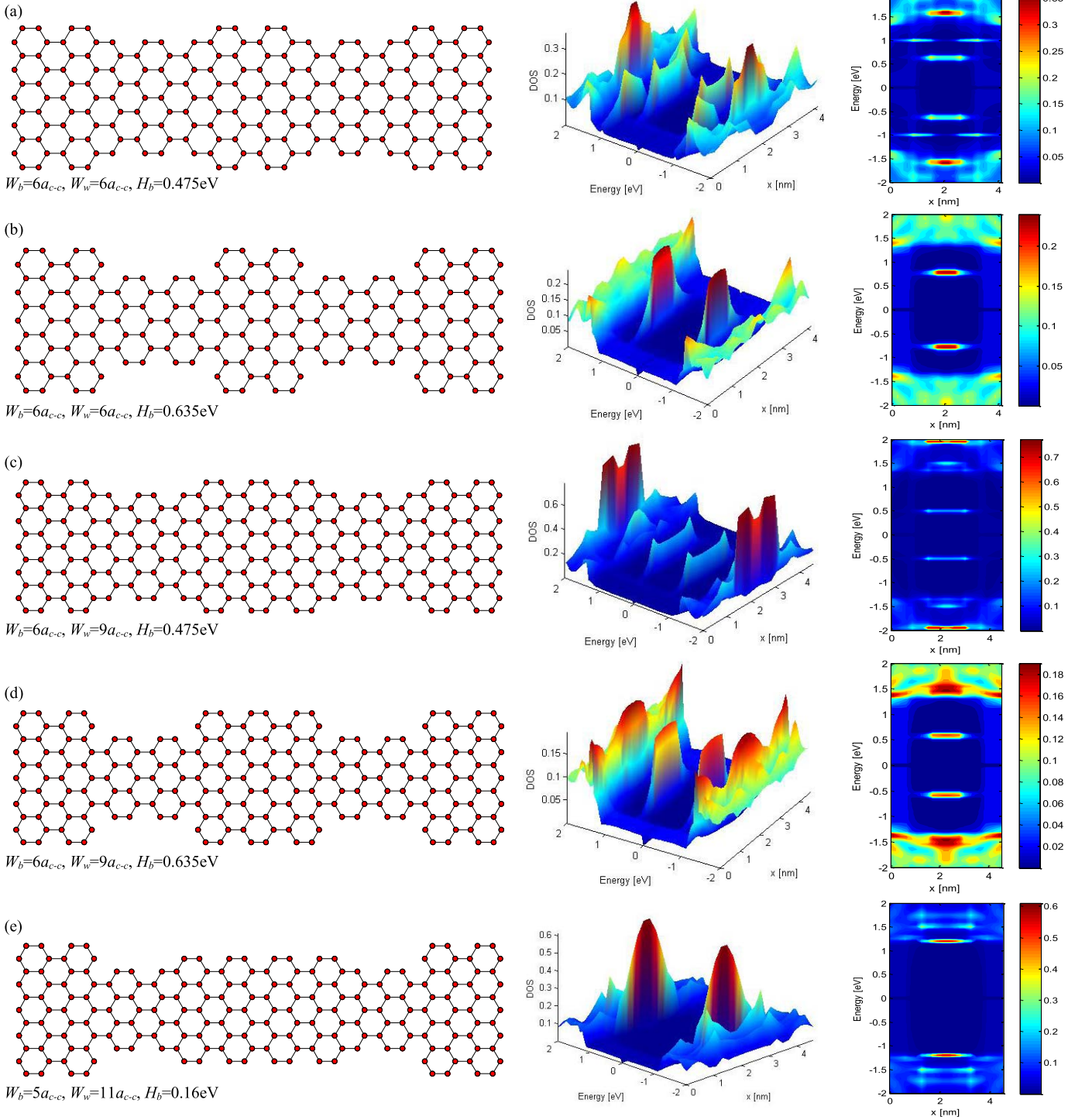
This article has been accepted for inclusion in a future issue of this journal. Content is final as presented, with the exception of pagination.

SAHA *et al.*: GNR QW INTERBAND AND INTERSUBBAND PHOTODETECTOR

5

Fig. 5.   Different A-GNR-QW structures with the variation of well width (W_w), barrier width (W_b), and barrier height (H_b). The corresponding DOS is also shown in 3-D and 2-D plots for $V_g = 0$ V and $V_d = 0$ V. (a) A-GNR-QW structure-1: $N_b = 9$ [$E_g = \sim 0.95$ eV] and $N_w = 11$ [$E_g = \sim 0$ eV]. (b) A-GNR-QW structure-2: $N_b = 7$ [$E_g = \sim 1.27$ eV] and $N_w = 11$ [$E_g = \sim 0$ eV]. (c) A-GNR-QW structure-3: $N_b = 9$ [$E_g = \sim 0.95$ eV] and $N_w = 11$ [$E_g = \sim 0$ eV]. (d) A-GNR-QW structure-4: $N_b = 7$ [$E_g = \sim 1.27$ eV] and $N_w = 11$ [$E_g = \sim 0$ eV]. (e) A-GNR-QW structure-5: $N_b = 7$ [$E_g = \sim 1.27$ eV] and $N_w = 9$ [$E_g = \sim 0.95$ eV].

photocurrent for optical transition (iii). A small PED [in Fig. 4(b)], and hence photoresponse with smaller peak, is obtained for optical transition (ii), as shown in Fig. 2(e). Though such transition is not supported by the conventional selection rules for ideal QW structures, here, small photoresponse is found due to the small size of the well (as it contains only a few number of atoms) where the shape of molecular orbitals within the well depends on its atomic orbitals rather than envelop wave function.

Different A-GNR-QW structures and their corresponding DOS are shown in Fig. 5 to analyze the effects of barrier height, barrier width, well length, and bandgap in energy

This article has been accepted for inclusion in a future issue of this journal. Content is final as presented, with the exception of pagination.
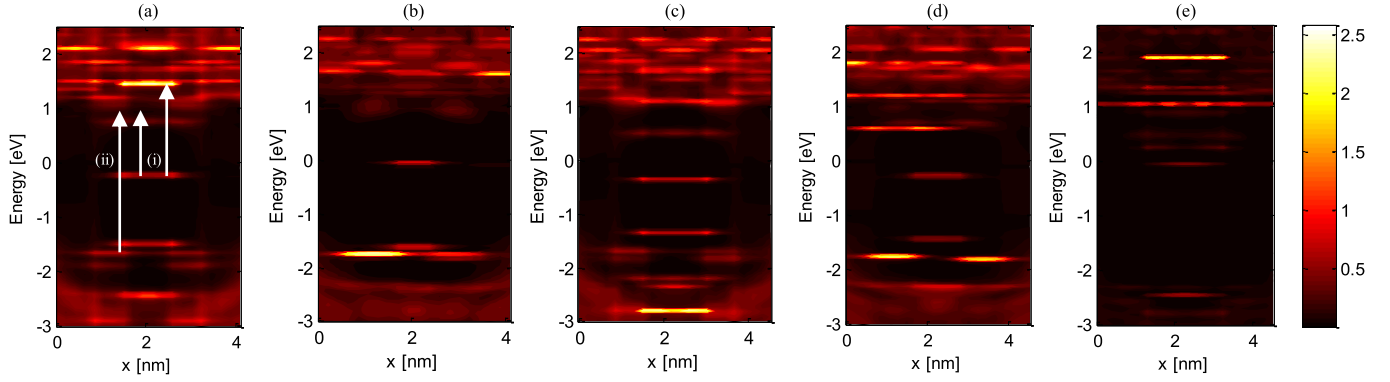
6

IEEE TRANSACTIONS ON ELECTRON DEVICES

Fig. 6. DOS of the different A-GNR-QW structures (shown in Fig. 3) under the back-gate voltage $V_g = 0.8$ V and drain voltage $V_d = 0.1$ V. Due to back-gate voltage, the first confined energy states within the CB populates by the electron, which in turn initiate intersubband transitions. (a) A-GNR-QW structure-1. (b) A-GNR-QW structure-2. (c) A-GNR-QW structure-3. (d) A-GNR-QW structure-4. (e) A-GNR-QW structure-5.
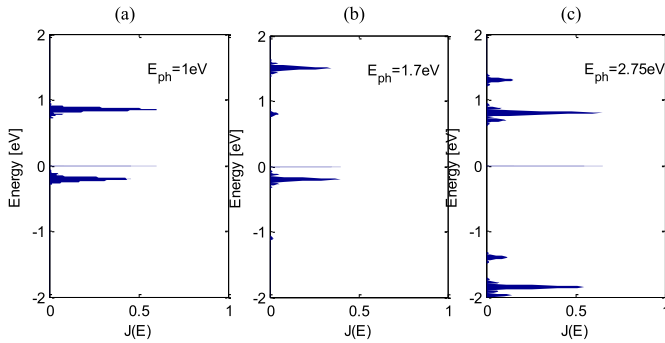

Fig. 7. (a)–(c) Normalized photocurrent spectra of A-GNR-QW structure-1 due to different photon energies when $V_g = 0.8$ V and $V_d = 0.1$ V.

state confinement in the well region. In Fig. 5(a)–(d), well is made of $N_w = 11$ A-GNR having a bandgap of ~0 eV. Comparing with their corresponding DOS, we can say that the confined state goes to a higher energy level due to the increment in barrier height, H_b, and goes to a lower energy level due to the increment in well width, W_w, whereas in Fig. 5(e), well is made of $N_w = 9$ A-GNR having a bandgap of ~0.95 eV, resulting in merged confined and quasi-continuous states. Fig. 6(a)–(e) shows the DOS of these A-GNR-QW structures at $V_g = 0.8$ V and $V_d = 0.1$ V. Due to the applied back-gate voltage, the first confined states in the CB go below the Fermi level and thus get populated. Normalized photocurrent current spectra of A-GNR-QW structure-1 for different photon energies under gate bias (0.8 V) are shown in Fig. 7. Moreover, under such bias condition, total photocurrent conservation along the x-direction also obeys for particular incident photon, as shown in Fig. 3(b). In order to assess their performances as a photodetector, Q.E. is calculated as

$$Q.E.(\%) = \frac{I_{\text{ph}}}{q * (P_{\text{total}}/E_{\text{ph}})} \times 100\% \qquad (14)$$

where P_{total} is the total incident optical power (in watt).

Fig. 8(a)–(e) shows the Q.E. of the simulated structures at $V_g = 0$ V and different drain bias voltages. Peaks are observed for the allowable interband optical transitions. Multiple peaks can occur in the Q.E. graphs (e.g., for structures-1–4). This is due to the presence of both the confined states and the
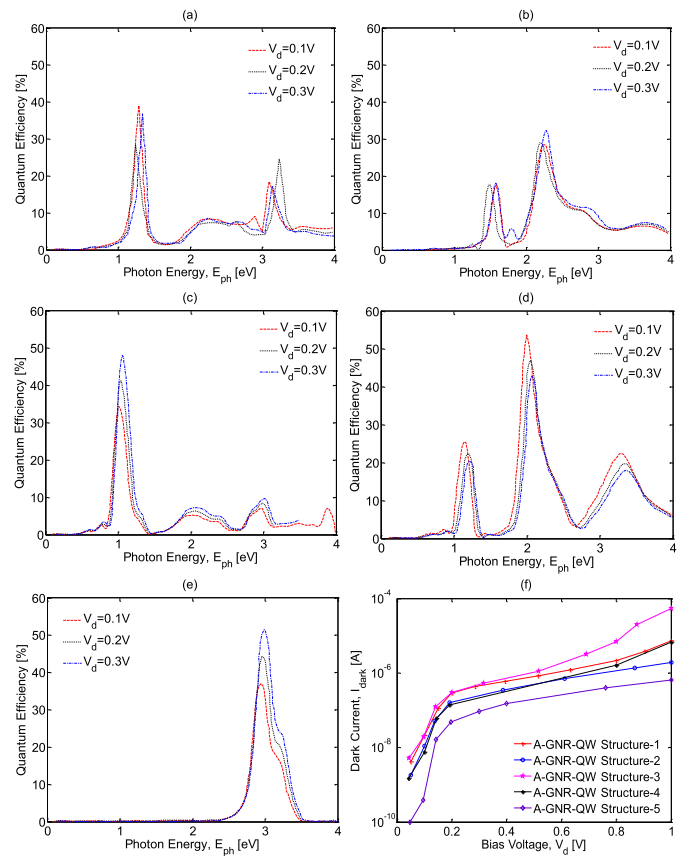

Fig. 8. (a)–(e) Q.E. of A-GNR-QW structure-1–5, respectively, under bias voltage of 0.1, 0.2, and 0.3 V when back $V_g = 0$. (f) Dark current at different drain bias voltages when $V_g = 0$.

quasi-continuous states, as shown in Fig. 5, in the well region of these structures. Therefore, there can be three different types of optical transitions, as discussed in Section I, resulting in multiple peaks in these spectra. On the other hand, for structure-5, as the confinement occurs at edge of continuum in both the CB and the VB, we get a single peak in the Q.E. spectrum.

When bias voltage is increased, the probability of electron tunneling from the source contact to the drain contact through

TABLE II
OPERATIONAL RANGE OF DIFFERENT A-GNR-QW PHOTODETECTORS

A-GNR-QW Photodetector	Interband (V_g = 0V)				Intersubband (V_g = 0.8V)			
	Photon Energy (eV)	Wavelength (nm)	Optical detection	Q.E. (%)	Photon Energy (eV)	Wavelength (nm)	Optical detection	Q.E. (%)
Structure-1	1.3	954	Near –infrared	38	1	1240	Near –infrared	31
	3.1	400	visible range(violet)	18	2.75	450	visible range(blue)	23
Structure-2	1.65	750	visible range(red)	20	1.3	954	Near –infrared	19
	2.2	564	visible range(green)	30	3	413	visible range(violet)	16
Structure-3	1.05	1181	Near –infrared	34	0.85	1459	Short-wavelength infrared (SWIR)	38
Structure-4	1.1	1127	Near –infrared	27	1	1240	Near –infrared	45
	2	620	visible range(red)	52	3.5	354	Ultraviolet (UV)	20
	3.3	375	Ultraviolet (UV)	22				
Structure-5	3	413	visible range(violet)	35	3.35	370	Ultraviolet (UV)	36

the barrier also increases. In the absence of incident photon, this tunneling current in the device for drain-to-source biasing is termed dark current, which is constant over the whole device. At relatively larger bias, electrons may gain larger energy than the barrier height and transmit through quasi-continuous or higher transmission states, resulting in larger dark current.

Fig. 8(f) shows dark current for different A-GNR-QW structures at $V_g = 0$ V. The current–voltage characteristics can be explained from the DOS plots of Fig. 5. Among various structures, for structure-3, shown in Fig. 5(c), the confined states are created in the nearest position of source Fermi level (∼0 eV), while for structure-5, shown in Fig. 5(e), the position of confined states is the furthest. Thus, for structure-3, with the increase of drain bias, larger dark current due to tunneling is observed, whereas for structure-5, observed dark current is relatively smaller. For three other structures, dark current is larger than structure-5 but smaller than structure-3, which is consistent with the relative position of the confined states in their corresponding DOS plots. One notable aspect is that the photodetector must be operated under a small drain bias for efficient operation, as dark current dominates over photocurrent at higher bias (>0.3 V).

As the application of back-gate voltage can populate the confined state of CB, for incident photons with relatively lower energies, photoresponse is found for optical transitions from this filled confined energy state to empty quasi-continuous states of CB, i.e., intersubband transitions. For example, in structure-1 [in Fig. 6(a)], optical transitions of type (i) and type (ii) [Fig. 1(c)] occur for particular incident photon energies. Hence, several peaks are observed in the corresponding Q.E. curve in Fig. 9(a). Here, the first peak (at ∼1 eV) and the second peak (at ∼1.7 eV) are due to intersubband transition (i), while the third peak (at ∼2.75 eV) is due to interband transition (ii). This claim is validated by the corresponding photocurrent spectra in Fig. 7. Similar argument can be presented for the observed peaks in Q.E. curves in Fig. 9(b)–(d) for structues-2–4. In these structures, for photon energies up to 2 eV, Q.E. peaks occur for intersubband transitions, while higher energy peaks occur for interband transitions.
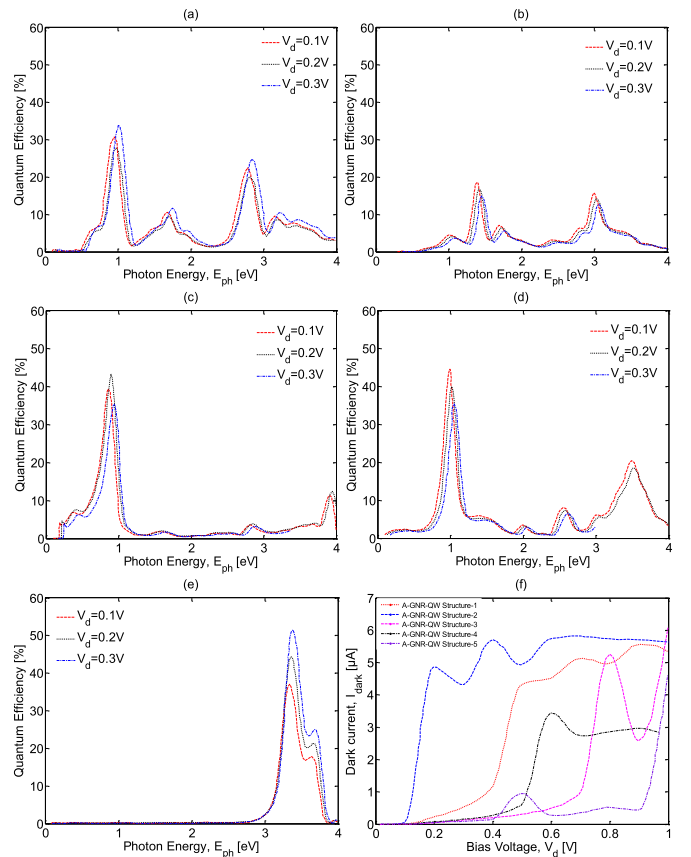

Fig. 9. (a)–(e) Q.E. of GNR structure-1–5, respectively, under bias voltage of 0.1, 0.2, and 0.3 V. The back-gate voltage $V_g = 0.8$ V. (f) Dark current at different drain bias voltages when $V_g = 0.8$ V.

A-GNR-QW structure-5 has no strictly confined states in the QW region; hence, it is not possible to populate any confined CB state under the applied bias. It is evident from Figs. 6(e) and 9(e) that the Q.E. peak for this structure is for interband transition. The application of back-gate voltage only shifts the photodetection peak.

Dark currents for the different A-GNR-QW structures at $V_g = 0.8$ V are shown in Fig. 9(f). At low drain bias (∼0.2 V), dark current is much larger in structure-2 than in structure-5, because under the specified bias condition, the confined state

This article has been accepted for inclusion in a future issue of this journal. Content is final as presented, with the exception of pagination.

8   IEEE TRANSACTIONS ON ELECTRON DEVICES

of CB of structure-2 goes below the Fermi level [in Fig. 6(b)], and thus electrons from the source contacts can readily tunnel to the drain contact through this state producing larger currents. While for structure-5, the confined state of CB is far away from zero energy level [in Fig. 6(e)], and thus lower dark current is obtained. For this reason, Q.E. is much lower in structure-2 than in structure-5. In addition, due to the pulling down of confined states of CB at level of contacts' states, resonant tunneling behavior is obtained in the dark current characteristics for designed A-GNR-QW structures (except for structure-5).

The summary of optical detection ranges and quantum efficiencies of various A-GNR-QW structures analyzed is presented in Table II. One of the interesting features is that an optical detection range of such photodetectors can be tuned from short-wavelength infrared (SWIR) to ultraviolet (UV) by: 1) varying structure of the photodetection layer and 2) applying appropriate back-gate voltages. Therefore, for a wide range of photodetection applications, one can either use the same structure with different back-gate voltages or use different QW structures with a specified back-gate voltage. Another important feature is that multicolor detection (from multiple peaks in the Q.E. curves of Figs. 8 and 9) is possible by this device. By comparing different quantum efficiencies of the structures, it is evident that Q.E. depends on the device structure and applied drain voltage. Therefore, a wide range of photodetection and multicolor photodetection with higher Q.E. is achievable through A-GNR-based QW photodetectors.

V. Conclusion

In this paper, we have studied different A-GNR QW structures to investigate the energy state confinement and their possible applications as a photodetector. We have proposed a device structure to get control over interband and intersubband optical transitions using a back-gate potential. The Q.E., dark current, and optical detection range for different A-GNR-QW structures have also been studied using the standard simulation approach. The results indicate that such photodetector can be tuned from the SWIR to the UV range along with single to multicolor detection. We expect that such A-GNR-QW structure-based device leads to useful applications in all-carbon optoelectronics.

References

[1] S. Dutta and S. K. Pati, "Novel properties of graphene nanoribbons: A review," *J. Mater. Chem.*, vol. 20, no. 38, pp. 8207–8223, Jun. 2010.

[2] V. Barone, O. Hod, and G. E. Scuseria, "Electronic structure and stability of semiconducting graphene nanoribbons," *Nano Lett.*, vol. 6, no. 12, pp. 2748–2754, Nov. 2006.

[3] D. Prezzi, D. Varsano, A. Ruini, A. Marini, and E. Molinari, "Optical properties of graphene nanoribbons: The role of many-body effects," *Phys. Rev. B*, vol. 77, no. 4, p. 041404, Jan. 2008.

[4] L. Yang, M. L. Cohen, and S. G. Louie, "Excitonic effects in the optical spectra of graphene nanoribbons," *Nano Lett.*, vol. 7, no. 10, pp. 3112–3115, Sep. 2007.

[5] C. Cocchi, D. Prezzi, A. Ruini, M. J. Caldas, and E. Molinari, "Optical properties and charge-transfer excitations in edge-functionalized all-graphene nanojunctions," *J. Phys. Chem. Lett.*, vol. 2, no. 11, pp. 1315–1319, May 2011.

[6] E. J. H. Lee, K. Balasubramanian, R. T. Weitz, M. Burghard, and K. Kern, "Contact and edge effects in graphene devices," *Nature Nanotechnol.*, vol. 3, no. 8, pp. 486–490, Jun. 2008.

[7] X. Xu, N. M. Gabor, J. S. Alden, A. M. van der Zande, and P. L. McEuen, "Photo-thermoelectric effect at a graphene interface junction," *Nano Lett.*, vol. 10, no. 2, pp. 562–566, Nov. 2010.

[8] M. C. Lemme et al., "Gate-activated photoresponse in a graphene p-n junction," *Nano Lett.*, vol. 11, no. 10, pp. 4134–4137, Aug. 2011.

[9] G. Konstantatos et al., "Hybrid graphene–quantum dot phototransistors with ultrahigh gain," *Nature Nanotechnol.*, vol. 7, no. 6, pp. 363–368, May 2012.

[10] Y.-W. Son, M. L. Cohen, and S. G. Louie, "Energy gaps in graphene nanoribbons," *Phys. Rev. Lett.*, vol. 97, no. 21, p. 216803, Nov. 2006.

[11] L. Yang, C.-H. Park, Y.-W. Son, M. L. Cohen, and S. G. Louie, "Quasiparticle energies and band gaps in graphene nanoribbons," *Phys. Rev. Lett.*, vol. 99, no. 18, p. 186801, Nov. 2007.

[12] M. Y. Han, B. Özyilmaz, Y. Zhang, and P. Kim, "Energy band-gap engineering of graphene nanoribbons," *Phys. Rev. Lett.*, vol. 98, no. 20, p. 206805, May 2007.

[13] P. Kim, M. Y. Han, A. F. Young, I. Meric, and K. L. Shepard, "Graphene nanoribbon devices and quantum heterojunction devices," in *Proc. IEEE Int. Electron Devices Meeting*, Dec. 2009, pp. 1–4.

[14] H. Sevinçli, M. Topsakal, and S. Ciraci, "Superlattice structures of graphene-based armchair nanoribbons," *Phys. Rev. B*, vol. 78, no. 24, p. 245402, Dec. 2008.

[15] S. Blankenburg et al., "Intraribbon heterojunction formation in ultranarrow graphene nanoribbons," *ACS Nano*, vol. 6, no. 3, pp. 2020–2025, Feb. 2012.

[16] Y.-C. Chen et al., "Molecular bandgap engineering of bottom-up synthesized graphene nanoribbon heterojunctions," *Nature Nanotechnol.*, vol. 10, no. 2, pp. 156–160, Jan. 2015.

[17] Q. Gao and J. Guo, "Quantum mechanical simulation of graphene photodetectors," *J. Appl. Phys.*, vol. 112, no. 8, p. 084316, Oct. 2012.

[18] M. Moradinasab, M. Pourfath, M. Fathipour, and H. Kosina, "Numerical study of graphene superlattice-based photodetectors," *IEEE Trans. Electron Devices*, vol. 62, no. 2, pp. 593–600, Feb. 2015.

[19] M. Ezawa, "Peculiar width dependence of the electronic properties of carbon nanoribbons," *Phys. Rev. B*, vol. 73, no. 4, p. 045432, Jan. 2006.

[20] S. Datta, "Nanoscale device modeling: The Green's function method," *Superlattices Microstruct.*, vol. 28, no. 4, pp. 253–278, Oct. 2000.

[21] M. Pourfath, *The Non-Equilibrium Green's Function Method for Nanoscale Device Simulation*. Vienna, Austria: Springer-Verlag, 2014.

[22] V. Perebeinos, J. Tersoff, and P. Avouris, "Effect of exciton-phonon coupling in the calculated optical absorption of carbon nanotubes," *Phys. Rev. Lett.*, vol. 94, no. 2, p. 027402, Jan. 2005.

[23] A. H. C. Neto, F. Guinea, N. M. R. Peres, K. S. Novoselov, and A. K. Geim, "The electronic properties of graphene," *Rev. Mod. Phys.*, vol. 81, no. 1, p. 109, Jan. 2009.

[24] J. Guo, S. Datta, M. Lundstrom, and M. P. Anantam, "Toward multiscale modeling of carbon nanotube transistors," *Int. J. Multiscale Comput. Eng.*, vol. 2, no. 2, pp. 257–276, 2004.

[25] L. E. Henrickson, "Nonequilibrium photocurrent modeling in resonant tunneling photodetectors," *J. Appl. Phys.*, vol. 91, no. 10, pp. 6273–6281, May 2002.

[26] U. Aeberhard and R. H. Morf, "Microscopic nonequilibrium theory of quantum well solar cells," *Phys. Rev. B*, vol. 77, no. 12, p. 125343, Mar. 2008.

[27] R. Venugopal, Z. Ren, S. Datta, M. S. Lundstrom, and D. Jovanovic, "Simulating quantum transport in nanoscale MOSFETs: Real versus mode space approaches," *J. Appl. Phys.*, vol. 92, pp. 3730–3739, Oct. 2002.

[28] U. Aeberhard, "Quantum-kinetic theory of steady-state photocurrent generation in thin films: Coherent versus incoherent coupling," *Phys. Rev. B*, vol. 89, no. 11, p. 115303, Mar. 2014.

Atanu K. Saha (M'15) received the B.Sc. and M.Sc. degrees in EEE from the Bangladesh University of Engineering and Technology, Dhaka, Bangladesh, in 2013 and 2015, respectively.

He has been a Faculty Member with the Electrical and Electronic Engineering Department, BRAC University, Dhaka, since 2013. His current research interests include numerical modeling of quantum transport in 2-D materials, III—V heterostructures, and nanophotonics.

Gobinda Saha (S'15) received the B.Sc. and M.Sc. degrees in EEE from the Bangladesh University of Engineering and Technology (BUET), Dhaka, Bangladesh, in 2013 and 2015, respectively.

He has been a Faculty Member with the Electrical and Electronic Engineering Department, BUET, since 2014. His current research interests include graphene-based high-speed low-power FET design, negative differential resistance device, and optical device design.

ABM Harun-ur Rashid (M'89–SM'02) received the B.Sc. degree in EEE from the Bangladesh University of Engineering and Technology (BUET), Bangladesh, in 1984, the M.Sc. degree in EE from Oita University, Japan, in 1988, and the Ph.D. in EE from The University of Tokyo, Japan, in 1996.

He served as a Design Engineer with Texas Instruments Japan Ltd., from 1988 to 1993. He was a Research Fellow with the Research Center for Nanodevices and Systems, Hiroshima University, Japan, from 2001 to 2003. He is currently a Professor with EEE Department, BUET.